Calorimetry at a Future Linear Collider

Steven Green
of Emmanuel College

A dissertation submitted to the University of Cambridge
for the degree of Doctor of Philosophy

Abstract

This thesis describes the optimisation of the calorimeter design for collider experiments at the future Compact LInear Collider (CLIC) and the International Linear Collider (ILC). The detector design of these experiments is built around high-granularity Particle Flow Calorimetry that, in contrast to traditional calorimetry, uses the energy measurements for charged particles from the tracking detectors. This can only be realised if calorimetric energy deposits from charged particles can be separated from those of neutral particles. This is made possible with fine granularity calorimeters and sophisticated pattern recognition software, which is provided by the PandoraPFA algorithm. This thesis presents results on Particle Flow calorimetry performance for a number of detector configurations. To obtain these results a new calibration procedure was developed and applied to the detector simulation and reconstruction to ensure optimal performance was achieved for each detector configuration considered.

This thesis also describes the development of a software compensation technique that vastly improves the intrinsic energy resolution of a Particle Flow Calorimetry detector. This technique is implemented within the PandoraPFA framework and demonstrates the gains that can be made by fully exploiting the information provided by the fine granularity calorimeters envisaged at a future linear collider.

A study of the sensitivity of the CLIC experiment to anomalous gauge couplings that effect vector boson scattering processes is presented. These anomalous couplings provide insight into possible beyond standard model physics. This study, which utilises the excellent jet energy resolution from Particle Flow Calorimetry, was performed at centre-of-mass energies of 1.4 TeV and 3 TeV with integrated luminosities of $1.5\mathrm{ab}^{-1}$

and 2ab^{-1} respectively. The precision achievable at CLIC is shown to be approximately one to two orders of magnitude better than that currently offered by the LHC.

Finally, a study into various technology options for the CLIC vertex detector is described.

Declaration

This dissertation is the result of my own work, except where explicit reference is made to the work of others, and has not been submitted for another qualification to this or any other university. This dissertation does not exceed the word limit for the respective Degree Committee.

Steven Green

Acknowledgements

Of the many people who deserve thanks, some are particularly prominent, such as my supervisor. . .

Contents

x

*"Writing in English is the most ingenious torture
ever devised for sins committed in previous lives."*
— James Joyce

Chapter 1

The sensitivity of CLIC to anomalous gauge couplings through vector boson scattering

"Kids, you tried your best, and you failed miserably. The lesson is, never try."

— Homer Simpson

1.1 Motivation

Vector boson scattering is the interaction of the form VV → VV where V is any of the electroweak gauge bosons W^+, W^-, Z or γ. This is an interesting process to study because it provides understanding of how the Standard Model Higgs is able to unitarise the otherwise unbounded cross section for longitudinal massive gauge boson scattering. Vector boson scattering also provides insights into beyond standard model physics that impacts the electroweak sector by probing potential anomalous triple and quartic gauge couplings.

Triple and quartic gauge couplings lead to interactions of the form V → VV and VV → VV respectively. In the Standard Model there are five allowed vertices, shown in figure 1.1, which arise from the kinematic term $\mathcal{L}_{kin} = -\frac{1}{4}B_{\mu\nu}B^{\mu\nu} - \frac{1}{4}W_{\mu\nu}W^{\mu\nu}$ in the Standard Model Lagrangian.
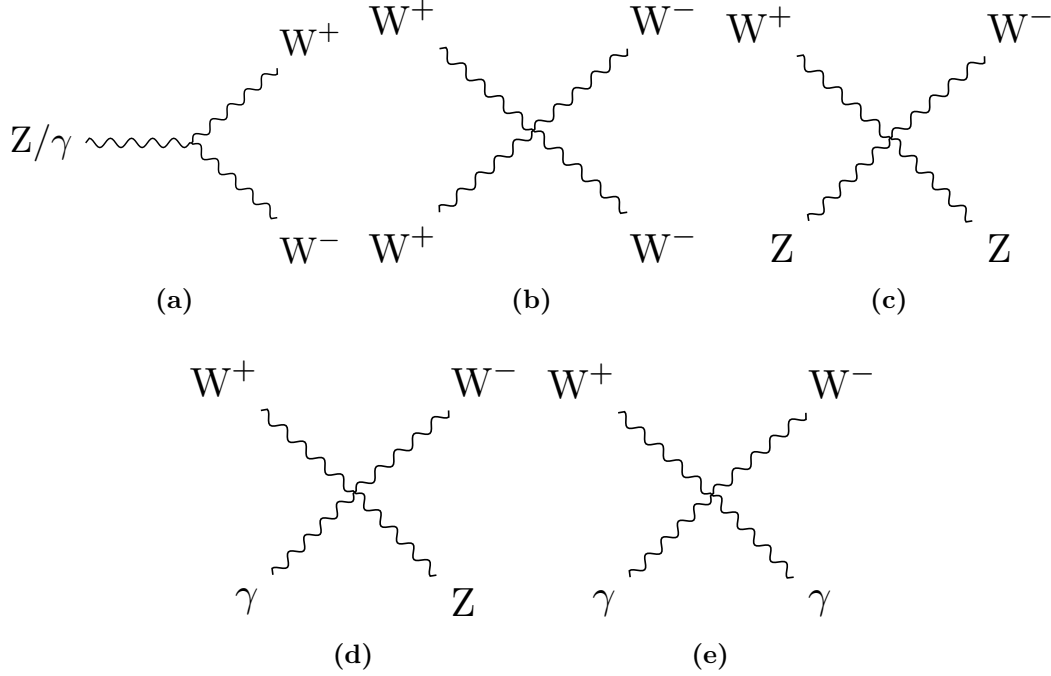
Figure 1.1: Triple and quartic gauge boson vertices in the Standard Model.

Anomalous triple and quartic gauge couplings are introduced as parameters in effective field theories (EFTs). These couplings either modify the Standard Model triple and quartic gauge boson vertices or introduce new triple and quartic vertices that were previously forbidden. EFTs are a mathematical construct designed to introduce new physics in a manner that builds upon the Standard Model. They work under the assumption that new physics exists at an energy scale, Λ, that is much higher than the energy scales currently accessible to modern day particle physics experiments. In the limit $\Lambda \to \infty$, the Standard Model is reproduced as the new physics becomes kinematically inaccessible. Such theories are model independent, giving them a wide span in the search for new physics. A classic example of an EFT theory is the Fermi theory for beta decay [1]. At energies much below the mass of the W boson, the weak interaction occurring when a neutron decays into a proton, electron and anti-neutrino can be treated as a four-point vertex with quartic coupling strength G_F, the Fermi Coupling constant as shown in figure 1.2.

The study presented in this chapter examines the anomalous quartic gauge couplings α_4 and α_5 through vector boson scattering process. The anomalous gauge couplings that are to be examined are introduced as part of an EFT that is described in chapter **??**.
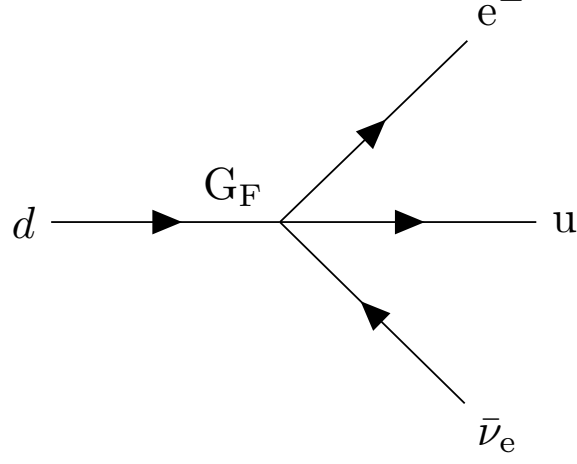
Figure 1.2: Four-point vertex proposed for explanation of beta decay by Fermi.

These couplings appear in the Lagrangian through the following terms:

$$\alpha_4[\text{Tr}(V^\mu V_\mu)]^2 \text{ and } \alpha_5 \text{Tr}(V^\mu V_\nu)]\text{Tr}(V^\nu V_\mu)], \tag{1.1}$$

where V_μ corresponds, in a carefully chosen gauge, to a linear combination of the massive gauge bosons W^+, W^- and Z. These terms modify the Standard Model vertices $W^+W^- \to W^+W^-$ and $W^+W^- \to ZZ$ as well as introducing the new vertex $ZZ \to ZZ$. The anomalous gauge couplings α_4 and α_5 can be studies in vector boson scattering processes such as those shown in figure 1.3.

CLIC is designed for precision measurements in e^+e^- collisions at high energies and it is ideal for a study of vector boson scattering. The application of Particle Flow Calorimetry with fine granularity calorimeters gives CLIC excellent jet energy resolution, which allows it to clearly characterise multi-jet final states and final states containing missing energy in the form of neutrinos. The excellent jet energy resolution also allows for accurate separation of W and Z bosons through di-jet invariant mass, which will be invaluable for event selection.

The cross sections for vector boson scattering processes are sufficiently large at the proposed running energies for CLIC to give large signal sample sizes. A study of anomalous gauge boson couplings at CLIC has the potential to give results several orders of magnitude better than the complementary studies performed at the LHC because of the reduction in hadronic backgrounds and increased cross section for vector boson
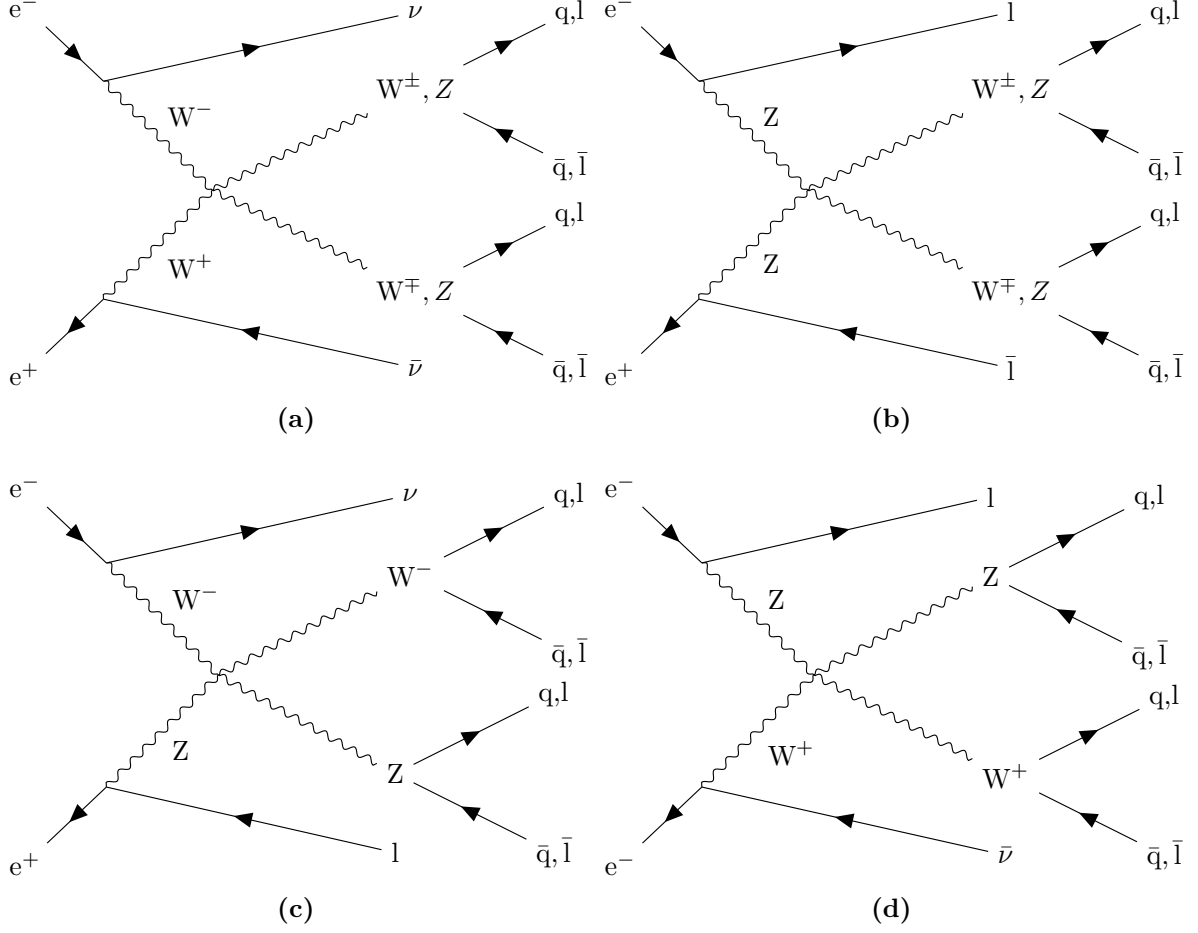
Figure 1.3: Example of vector boson scattering Feynman diagrams showing sensitivity to quartic gauge boson self-interaction vertices. The processes shown are relevant for CLIC. In these diagrams q represents the u, d, s, c and b quarks; l represents e^-, μ^- and τ^- leptons; and ν represents the ν_e, ν_μ and ν_τ neutrinos.

scattering processes [2]. The above reasons make a strong case for performing a vector boson scattering analysis at CLIC.

The branching fractions for the hadronic decays of both the $W^\pm$ and Z bosons is of the order of 70% [3], therefore, the signal final states for the analysis presented in this chapter are vector boson scattering processes where the outgoing bosons decay purely hadronically: $\nu\nu$qqqq, lνqqqq and llqqqq.

1.2 Event Generation, Simulation and Reconstruction

Events were generated using Whizard [4,5] version 1.95. Due to the presence of beam-strahlung photons in the CLIC beam, events were generated for collisions of e^+e^-, $e^+\gamma$, γe^- and $\gamma\gamma$. The energy spectra used for all particles involved in these collisions took into account the effects of radiation in the form of beamstrahlung photons and the intrinsic energy spread of the CLIC beam. Furthermore, events involving the interaction between the electromagnetic field of the beam particles involving quasi-real photon mediators with low momenta, described by the Weizsacker-Williams approximation or the Equivalent Photon Approximation (EPA), were generated using Whizard and included in this analysis. Fragmentation and hadronisation was implemented using PYTHIA 6.4 [6] that was tuned for OPAL e^+e^- collision data recorded at LEP [7]. The decays of tau leptons was simulated using TAUOLA [8]. The full list of events used in this analysis, along with their Standard Model cross section at $\sqrt{s} = 1.4$ TeV can be found in table 1.1. The samples comprise all final states that are relevant, either as signal or background processes, for an analysis involving the purely hadronic decay channels from the vector boson scattering process:

- Final states from the purely hadronic decay channels of the vector boson scattering process. These states are expected to show sensitivity to the anomalous couplings α_4 and α_5: $e^+e^- \rightarrow \nu\nu qqqq$, $e^+e^- \rightarrow l\nu qqqq$ and $e^+e^- \rightarrow llqqqq$

- Final states with four primary quarks arising from e^+e^- interactions: $e^+e^- \rightarrow qqqq$.

- Final states with two primary quarks arising from e^+e^- interactions: $e^+e^- \rightarrow \nu\nu qq$, $e^+e^- \rightarrow l\nu qq$, $e^+e^- \rightarrow llqq$ and $e^+e^- \rightarrow qq$.

- Final states with four primary quarks arising from the interactions of either e^+ or e^- with a beamstrahlung photon: $\gamma_{BS}e^- \rightarrow qqqqe^-$, $e^+\gamma_{BS} \rightarrow qqqqe^+$, $\gamma_{BS}e^- \rightarrow qqqq\nu$ and $e^+\gamma_{BS} \rightarrow qqqq\nu$.

- Final states with four primary quarks arising from the interactions of either e^+ or e^- with the electromagnetic field of the opposing beam particle. These cross sections are calculated using the EPA approximation, which represents the electromagnetic field of the opposing beam particle as a series of photons, so the final states appear as interactions of e^+ or e^- with photons: $\gamma_{EPA}e^- \rightarrow qqqqe^-$, $e^+\gamma_{EPA} \rightarrow qqqqe^+$, $\gamma_{EPA}e^- \rightarrow qqqq\nu$ and $e^+\gamma_{EPA} \rightarrow qqqq\nu$.

- Final states with four primary quarks arising from the interaction of the electromagnetic fields of opposing beam particles using the EPA approximation: $\gamma_{\text{EPA}}\gamma_{\text{EPA}} \rightarrow$ qqqq.

- Final states with four primary quarks arising arising from the interaction of the electromagnetic field of either e^+ or e^- using the EPA approximation with a beamstrahlung photon: $\gamma_{\text{EPA}}\gamma_{\text{BS}} \rightarrow$ qqqq or $\gamma_{\text{BS}}\gamma_{\text{EPA}} \rightarrow$ qqqq.

- Final states with four primary quarks arising from the interaction of two beamstrahlung photons: $\gamma_{\text{BS}}\gamma_{\text{BS}} \rightarrow$ qqqq.

In the above list q represents u, $\bar{\text{u}}$, d, $\bar{\text{d}}$, s, $\bar{\text{s}}$, c, $\bar{\text{c}}$, b or $\bar{\text{b}}$; l represents $e^\pm$, $\mu^\pm$ or $\tau^\pm$; and ν represents ν_{e}, $\overline{\nu}_{\text{e}}$, ν_μ, $\overline{\nu}_\mu$, ν_τ and $\overline{\nu}_\tau$.

Monte-Carlo (MC) samples were simulated using the CLID_ILD detector model [9]. Further details of this detector model can be found in chapter **??**. The simulation was performed in MOKKA [10], which is a GEANT4 [11] wrapper providing detailed geometric descriptions of detector concepts for the linear collider. Events were reconstructed using the MARLIN [12] c++ framework, designed for reconstruction at the linear collider. PandoraPFA [13,14] was used to apply Particle Flow Calorimetry in the reconstruction, the full details of which can be found in chapter **??**.

The effect of the $\gamma\gamma \rightarrow hadrons$ backgrounds, discussed in section **??**, were incorporated in the analysis by overlaying $\gamma\gamma \rightarrow hadrons$ events onto the signal and background event samples. The overlaid backgrounds were added prior to reconstruction so that their impact on the reconstruction was fully accounted for. For a given event, the exact number of background events overlaid is drawn from a Poisson distribution with a mean of 1.3 (3.2) events per bunch crossing at $\sqrt{s} = 1.4$ (3) TeV [15].

1.3 Modelling of Anomalous Gauge Couplings

The samples that were sensitive to the anomalous gauge couplings α_4 and α_5 were generated using Whizard version 1.97, instead of the previously quoted version 1.95. This change was required as version 1.97 contained a unitarisation scheme that ensured cross sections for processes involving longitudinal gauge boson scattering were bound at the energies considered here.

Final State	Cross Section $\sqrt{s} = 1.4$ TeV [fb]
$e^+e^- \to \nu\nu qqqq$	24.7
$e^+e^- \to l\nu qqqq$	110.4
$e^+e^- \to llqqqq$	62.1
$e^+e^- \to qqqq$	1245.1
$e^+e^- \to \nu\nu qq$	787.7
$e^+e^- \to l\nu qq$	4309.7
$e^+e^- \to llqq$	2725.8
$e^+e^- \to qq$	4009.5
$\gamma_{EPA}e^- \to qqqqe^-$	287.1
$\gamma_{BS}e^- \to qqqqe^-$	1160.7
$e^+\gamma_{EPA} \to qqqqe^+$	286.9
$e^+\gamma_{BS} \to qqqqe^+$	1156.3
$\gamma_{EPA}e^- \to qqqq\nu$	32.6
$\gamma_{BS}e^- \to qqqq\nu$	136.9
$e^+\gamma_{EPA} \to qqqq\nu$	32.6
$e^+\gamma_{BS} \to qqqq\nu$	136.4
$\gamma_{EPA}\gamma_{EPA} \to qqqq$	753.0
$\gamma_{EPA}\gamma_{BS} \to qqqq$	4034.8
$\gamma_{BS}\gamma_{EPA} \to qqqq$	4018.7
$\gamma_{BS}\gamma_{BS} \to qqqq$	21406.2

Table 1.1: Cross sections of signal and background processes at $\sqrt{s} = 1.4$ TeV. In the above table q represents u, $\bar{\text{u}}$, d, $\bar{\text{d}}$, s, $\bar{\text{s}}$, c, $\bar{\text{c}}$, b or $\bar{\text{b}}$; l represents $e^\pm$, $\mu^\pm$ or $\tau^\pm$; and ν represents ν_e, $\overline{\nu_e}$, ν_μ, $\overline{\nu_\mu}$, ν_τ and $\overline{\nu_\tau}$. The EPA and BS subscript on the incoming photon indicates whether the photon is generated from the equivalent photon approximation or beamstrahlung.

Two alternative methods exist for modelling the sensitive of the vector boson scattering process to the anomalous gauge couplings α_4 and α_5. The first is to generate multiple samples with different values of α_4 and α_5 and the second is to generate a single sample with $\alpha_4 = 0$ and $\alpha_5 = 0$ and reweight that sample. The latter approach was taken in this analysis as the former approach is impractical when considering a fine sampling of the α_4 and α_5 space.

Event weights, w, are calculated according to the ratio of the matrix elements, M, for the particular event configuration [16]

$$w(\alpha_4, \alpha_5) = \left(\frac{M(event, \alpha_4, \alpha_5)}{M(event, 0, 0)} \right)^2. \tag{1.2}$$

Figure 1.4 shows the dependence of the event weights on α_4 and α_5 for four selected $\sqrt{s} = 1.4$ TeV $\nu\nu qqqq$ final state events.

(a)

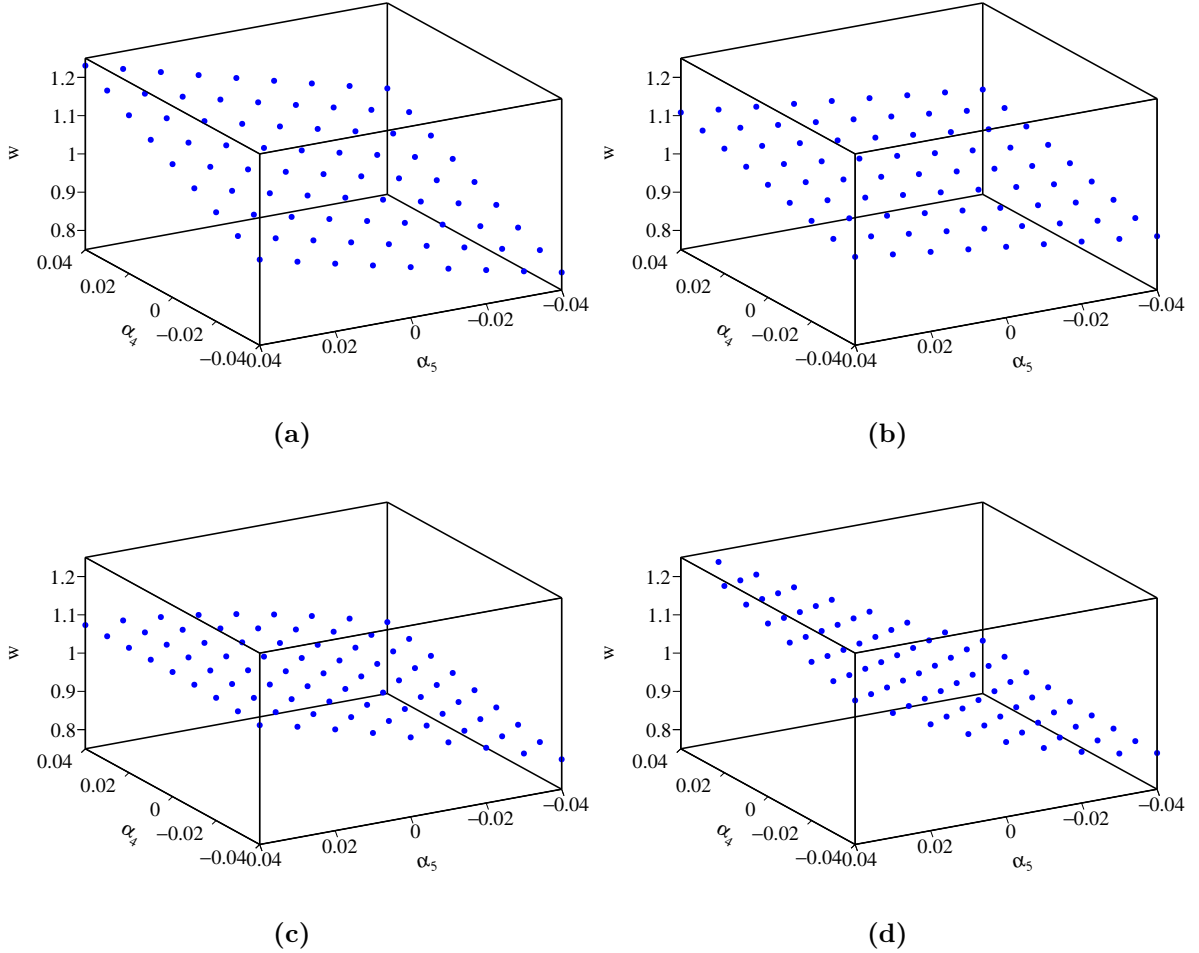**(b)**

(c)

(d)

Figure 1.4: The event weight as a function of the anomalous couplings α_4 and α_5 for a selection of $\nu\nu qqqq$ final state events at $\sqrt{s} = 1.4$ TeV.

Only final states involving contributions from massive gauge boson quartic vertices require reweighting. Whizard was used to evaluate the cross sections for all final states shown in table 1.1 with $\alpha_4 = \alpha_5 = 0$ and with $\alpha_4 = \alpha_5 = 0.05$. Only the three final states shown in table 1.2 were found to have a dependency on α_4 and α_5.

Final State	Cross Section [fb] ($\alpha_4 = \alpha_5 = 0.00$)	Cross Section [fb] ($\alpha_4 = \alpha_5 = 0.05$)	Percentage Change[%]
$e^+e^- \rightarrow \nu\nu qqqq$	24.7	34.6	+40.1
$e^+e^- \rightarrow l\nu qqqq$	115.3	113.0	-2.0
$e^+e^- \rightarrow llqqqq$	62.1	68.6	+10.5

Table 1.2: Cross sections for selected processes showing the effect of the anomalous gauge couplings α_4 and α_5 at $\sqrt{s} = 1.4$ TeV.

To maximise the sensitivity to the anomalous gauge couplings, the $\nu\nu qqqq$ final state is used to define signal in this analysis. The $l\nu qqqq$ and $llqqqq$ final states are treated as backgrounds that are invariant to changes in α_4 and α_5 because they have a much reduced sensitivity to the anomalous gauge couplings in comparison to the $\nu\nu qqqq$ final state. Furthermore, the $l\nu qqqq$ and $llqqqq$ final states can be easily vetoed during event selection, because to the presence of the primary lepton, which means the sensitivity of these states to the anomalous gauge couplings will have a negligible effect on the results from this study.

Modelling of the anomalous gauge coupling α_4 and α_5 in Whizard enforces a unit CKM matrix. No significant differences were observed when comparing a number of reconstructed level distributions for $\nu\nu qqqq$ final state events generated with Whizard using a Standard Model and unit CKM matrix, which indcates that enforcing a unit CKM matrix had a negligible effect on this analysis.

1.4 Data Analysis

The following section contains a description of how the variables used throughout the anomalous gauge coupling sensitivity study are determined.

1.4.1 Limiting Beam Related Backgrounds

During the reconstruction, after the inner detector tracks have been reconstructed, the CLICTrackSelection processor is applied, which vetoes poorly reconstructed and fake tracks by applying simple quality cuts to the number of hits in the tracking sub-detectors. The CLICTrackSelection processors also reject tracks where the time of arrival at the

calorimeter differs by more than 50 ns between a straight line of flight and a helix fit to the track. Applying this cut ensures that associations made between charged particles tracks and calorimetric energy deposits are consistent.

Following the reconstruction, the CLICPfoSelector processor is applied to remove reconstructed particle flow objects (PFOs) that originate from beam related backgrounds. This processor applies cuts on the p_T and timing information of the PFOs, which vary as a function of position in the detector and the PFO type to target regions of the detector where backgrounds are more prominent, e.g. low p_T for $\gamma\gamma \rightarrow hadrons$ events. Three configurations of the CLICPfoSelector have been developed for the CLIC environment and were considered in this analysis. They are, in order of increasing background rejection, the Loose, Default and Tight selections [14].

1.4.2 Jet Finding

After the application of the CLICPfoSelector, the MarlinFastJet processor, a wrapper for the FastJet [17] processor, was used to cluster each event into four jets. These jets are then paired up to form two candidate bosons working under the assumption that the correct pairing is achieved when the difference between the invariant masses of the candidate bosons is a minima. In the case of the signal final state, $\nu\nu$qqqq, it is assumed that the four jets and two candidate bosons map onto the four primary quarks and two outgoing bosons in the vector boson scattering process. The jet clustering was performed using the longitudinally invariant k_t jet algorithm in exclusive mode. The longitudinally invariant k_t algorithm proceeds as follows

1. Determine the k_t distance, d_{ij}, for each pair of particles, i and j, and the beam, d_{iB}, distance for each particle, i. These distances are defined as

$$d_{ij} = \min(p_{ti}^2, p_{tj}^2)\Delta R_{ij}^2 / R^2 \ , \tag{1.3}$$

$$d_{iB} = p_{ti}^2 \ , \tag{1.4}$$

   where $\Delta R_{ij}^2 = (y_i - y_j)^2 + (\phi_i - \phi_j)^2$, p_{ti} is the transverse momentum of particle i, y_i is the rapidity of particle i, ϕ_i is the azimuthal angle of the direction of travel of particle i and R is a configurable parameter that typically is of the order of 1.

2. Find the minimum distance, $d_{\min}$, of all the k_t and beam distances. If the minimum occurs for a k_t distance, particles i and j are merged, summing their 4-momenta. If

the beam distance is the minima, particle i was declared to be part of the "beam" jet and the particle is removed from the list of particles and not included in the final jet output.

3. Repeat until the desired number of jets is created. Alternatively, in inclusive mode this would be repeated until no particles are left in the event.

Two other clustering algorithms were considered, but, as figure 1.5 shows, were found to be inappropriate for the experimental conditions at CLIC. These alternative algorithm choices are applied in the same manner as the longitudinally invariant k_t algorithm, however, they differ in the definition of d_{ij} and d_{iB}.
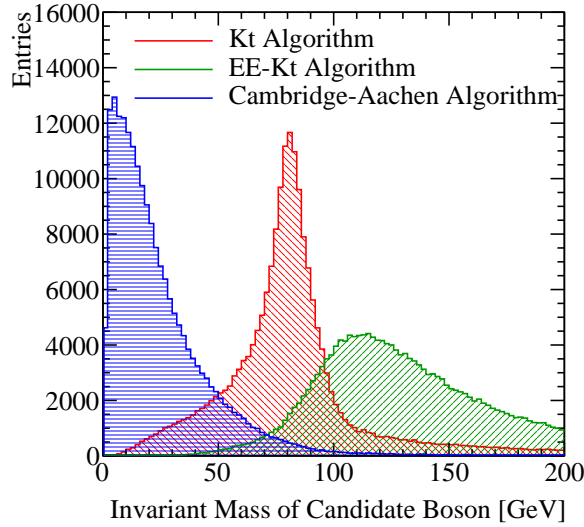

Figure 1.5: The reconstructed masses for different choices of jet algorithm for $\sqrt{s} = 1.4$ TeV $\nu\nu$qqqq final state events. The masses are determined by forcing the events into 4 jets and then pairing the jet pairs to form candidate bosons. The jet pairing configuration is determined by pairing jets such that the mass differences between the two candidate bosons is a minimum. These samples should be dominated by vector boson scattering involving pairs of outgoing W bosons and so it is expected that a peak at the W boson mass, $m_W = 80.385 \pm 0.015$ GeV [3], should be observed. As this does not occur for the Cambridge-Aachen algorithm or the EE_kt algorithm they were deemed unsuitable for this analysis. In the case of the kt algorithm and the EE_kt algorithm an R parameter of 0.7 was used.

The first alternative jet algorithm considered was the k_t algorithm for e$^+$e$^-$ colliders, the EE_kt or Durham algorithm. In this algorithm d_{iB} is not used and

$$d_{ij} = 2\min(E_i^2, E_j^2)(1 - cos\theta_{ij}) \; , \tag{1.5}$$

where θ_{ij} is the opening angle of particles i and j and E_i is the energy of particle i. In the collinear limit d_{ij} corresponds to the relative transverse momenta of the particles. The major failure of this algorithm when applied to CLIC is the absence of d_{iB}, which leads to large numbers of beam related background particles being associated to jets. As figure 1.5 shows, the invariant mass of the paired jets, which should peak around the W and Z boson masses, is much larger than expected, due to the presence of these backgrounds. Also this algorithm is not invariant to boosts along the beam direction meaning that it is inappropriate for use at CLIC given the beam induced backgrounds modify the nominal collision kinematics.

The second alternative jet algorithm considered was the Cambridge-Aachen jet algorithm where

$$d_{ij} = \Delta R_{ij}^2 / R^2 \ , \tag{1.6}$$

$$d_{iB} = 1 \ . \tag{1.7}$$

This algorithm performs poorly as it does not accounts for the transverse momentum or the energy of the particles being clustered. In essence, this is a cone clustering algorithm with a cone radius defined through $\Delta R_{ij} = R$, which even for large R was found to discard too much energy in the event to be useful for this analysis. This can be seen in figure 1.5 where the invariant mass of the paired jets is much lower than expected. This algorithm is appropriate for events that contain highly boosted jets, however, at CLIC the jets are too disperse for this algorithm to be successful.

1.4.2.1 Optimal Jet Finding Algorithm

Optimisation of the jet finding procedure was performed on both the PFO selection and the value of the R parameter used in the longitudinally invariant k_t algorithm. The optimal configuration for the jet algorithm at $\sqrt{s} = 1.4$ TeV was found to use default selected PFOs and an R parameter of 0.9.

The optimisation procedure involved performing the sensitivity study, described in section 1.6, using solely the $\nu\nu$qqqq signal final state. This methodology ensures that the optimisation was done with respect to the physics of interest without having to perform the jet reconstruction for the large number of background events for each jet algorithm configuration considered.

Figure 1.6a shows confidence contours, given a null hypothesis of $\alpha_4 = \alpha_5 = 0$, for the optimal jet configuration at $\sqrt{s} = 1.4$ TeV. Figures 1.6b and 1.6c show the one dimensional χ^2 distribution for α_4 and α_5, assuming $\alpha_5 = 0$ and $\alpha_4 = 0$ respectively, for the optimal jet configuration at $\sqrt{s} = 1.4$ TeV. These distributions give one sigma confidence limits on the anomalous gauge couplings of

$$-0.0038 < \alpha_4 < 0.0047 \tag{1.8}$$

and

$$-0.0027 < \alpha_5 < 0.0030. \tag{1.9}$$

These confidence limits represent the idealised sensitivity of the CLIC experiment to the anomalous gauge couplings. Once the effects of backgrounds and event selection are included in the analysis, these confidence limits will increase in size.

1.4.3 Lepton Finding

An isolated lepton finder was included in the analysis chain to reject background final states containing primary leptons. Leptons produced via hadronisation are unlikely to be flagged as isolated because all hadronisation products are boosted along the direction of the parent quark. This means isolated leptons are likely to correspond to primary leptons, which makes the number of isolated leptons a powerful discriminating variable to use in event selection.

The isolated lepton finder determines whether a PFO is an electron or muon by first checking that the PFO has a single charged particle track associated to it. If that is the case, the calorimetric energy deposits of the PFO are examined to see if they are consistent with what is expected for an electron or muon. If they are consistent with expectations, the properties of the charged particle track are examined to determine whether the track originates from the IP. If the PFO is deemed to have originated from the IP, isolation checks, which examine the energy deposited in the calorimeters within a cone surrounding the PFO, are applied to determine whether the particles belongs to a jet. If the PFO does not appear to belong to a jet then it is counted as an isolated lepton. The efficiency of the lepton finder is summarised in table 1.3.
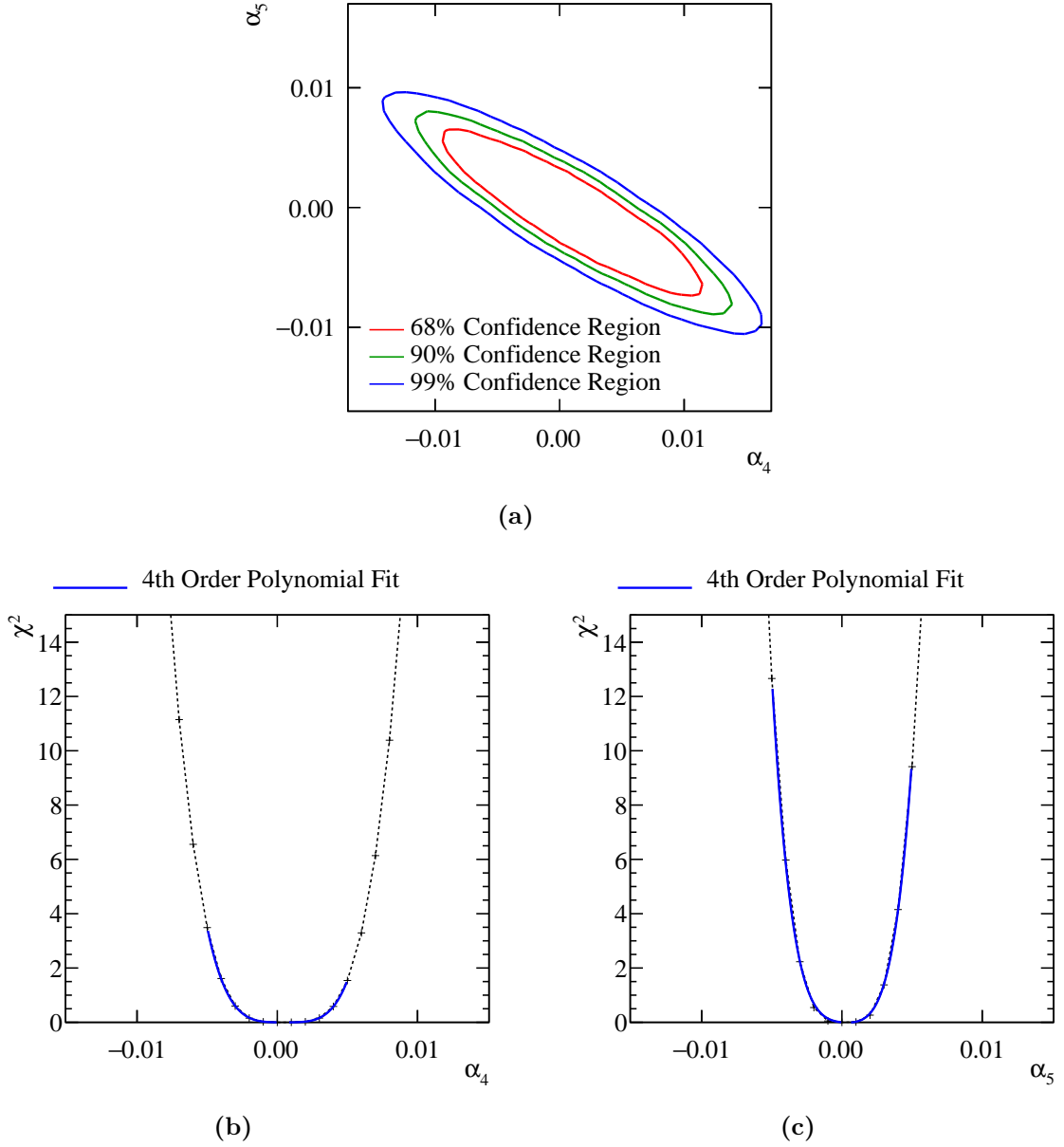
(a)

(b)

(c)

Figure 1.6: χ^2 sensitivity distributions from a fit to M_{VV} for the signal qqqq$\nu\nu$ final state only at $\sqrt{s} = 1.4$ TeV. These results use the optimal jet algorithm configuration of selected PFOs and an R parameter of 0.9 in the k_t algorithm. (a) χ^2 sensitivity contours in α_4 and α_5 space. (b) χ^2 as a function of α_4 assuming $\alpha_5 = 0$. (c) χ^2 as a function of α_5 assuming $\alpha_4 = 0$.

Final State	$\epsilon_{\text{Lepton Finding}}$
$e^+e^- \to \nu\nu qqqq$	99.7
$e^+e^- \to l\nu qqqq$	48.9

Table 1.3: The efficiency of isolated lepton finding at $\sqrt{s} = 1.4$ TeV for the $\nu\nu qqqq$ and $l\nu qqqq$ final states. Efficiency here is defined as the fraction of events where no isolated leptons were found.

1.4.4 Discriminant Variables

The next stage of the analysis involved the calculation of a number of event-based variables that were found to be useful for this analysis. The variables that were calculated are as follows

- **Particle level** variables:
    - Number of PFOs in each jet.
    - Energy of the highest energy PFO.
    - Energy of the highest energy electron.
    - Cosine of the polar angle of the highest energy track.
    - The number of isolated leptons found using the isolated lepton finder.

- **Candidate boson** variables:
    - Energy of the candidate bosons.
    - Invariant mass of the candidate bosons.
    - Acolinearity of the candidate boson pair, which is defined as 180 degrees minus the opening angle of the pair of bosons in the rest frame of the detector.

- **Event based** variables:
    - The invariant mass of the visible system, M_{VV}.
    - The vector sum of the transverse momentum of all PFOs in the event.

– Sphericity, defined through the sphericity tensor S^{ab}:

$$S^{ab} = \frac{\Sigma_i p_i^{\alpha} p_j^{\alpha}}{\Sigma_{i,\alpha=1,2,3}|p_{i|}^{\alpha 2}} \tag{1.10}$$

Where p_i are the components of the momenta of PFO i in the rest frame of the detector and the sum Σ_i runs over all particles in the event. Sphericity is defined as $S = \frac{3}{2}(\lambda_2 + \lambda_3)$, where λ_i are the eigenvalues of the sphericity tensor defined such $\lambda_1 \geq \lambda_2 \geq \lambda_3$. This provides a measure of how spherical the reconstructed event topology is with isotropic events having $S \approx 1$, while two jet events have $S \approx 0$.

- **Jet clustering parameters**, y_{ij} where $i = 3, 4$ and $j = i + 1$. These are the smallest k_t distance found when combining j jets into i jets.

1.4.5 Jet Energy Resolution at CLIC

The importance of the jet energy resolution that is extensively discussed in chapters **??** and **??** should be emphasised at this point. Many of the discriminant variables that are calculated for this analysis are dependant upon the jet energy resolution. In particular, all variables related to the candidate bosons that are formed from pairing up jets, are dependent upon the measurement of jet energies.

Figure 1.7 shows the jet energy resolution as a function of the MC jet energy for the $\nu\nu$qqqq event sample used in the $\sqrt{s} = 1.4$ TeV analysis. The MC jet energy was obtained by pairing up quarks appearing in the final state to the reconstructed jets. The events were then binned in terms of their MC jet energy and the jet energy resolution calculated for each bin. When calculating the jet energy resolution, a narrower range of jet energies was used in compared to previous studies, 60% of the data with narrowest RMS as opposed to 90%, to minimise the effects of jet finding and beam-induced backgrounds. The jet energy resolutions reported here are worse than those quoted in earlier chapters, however, this is to be expected given the effects of jet finding and beam-induced backgrounds.
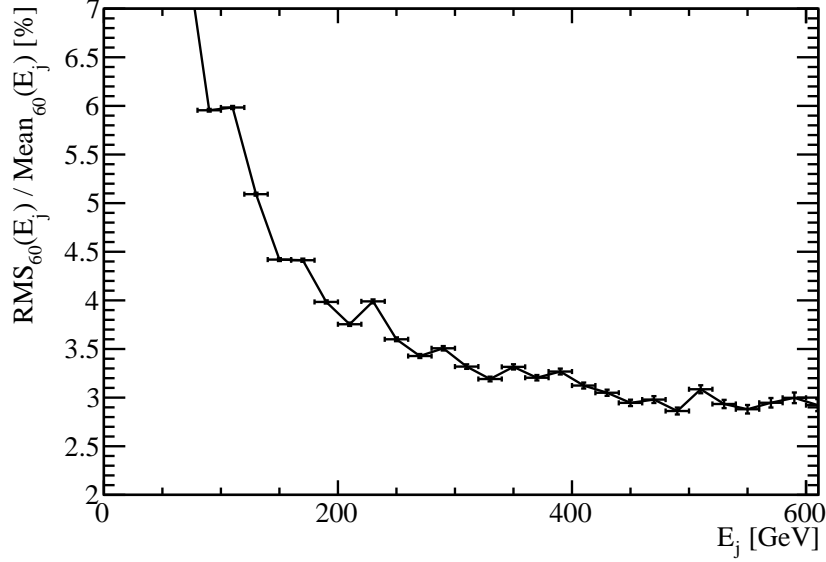
Figure 1.7: The jet energy resolution as a function of the jet energy for the $\nu\nu$qqqq final state at $\sqrt{s} = 1.4$ TeV.

1.5 Event Selection

This section discusses the event selection procedure that is applied in this analysis. The goal of this procedure is to isolate the $\nu\nu$qqqq final state from the backgrounds final states, i.e. those containing two and four primary quarks. The procedure consists of a set of preselection cuts followed by the application of a multivariate analysis (MVA). All event numbers used in this analysis have been normalised, prior to event selection, to an integrated luminosity ($\mathcal{L}_{int}$) of 1.5 (2) ab^{-1} for CLIC running at $\sqrt{s} = 1.4$ (3) TeV.

1.5.1 Preselection

A refined selection of the $\nu\nu$qqqq signal final state is achieved using MVA, however, to ensure efficiency in the training and application of that MVA a number of simple preselection cuts were developed to veto obvious background final states prior to the application of the MVA. Preselection cuts were applied to the transverse momentum of the system and the number of isolated leptons found in the event. The raw distributions of these variables is shown in figure 1.8 and based on these distributions the following cuts were applied

- Transverse momentum of system > 100 GeV. This cut is effective due to the presence of missing energy in the form of neutrinos in the signal final state.

- Number of isolated leptons in system = 0. This cut is effective as the signal final state does not contain leptons, while numerous background final states do.

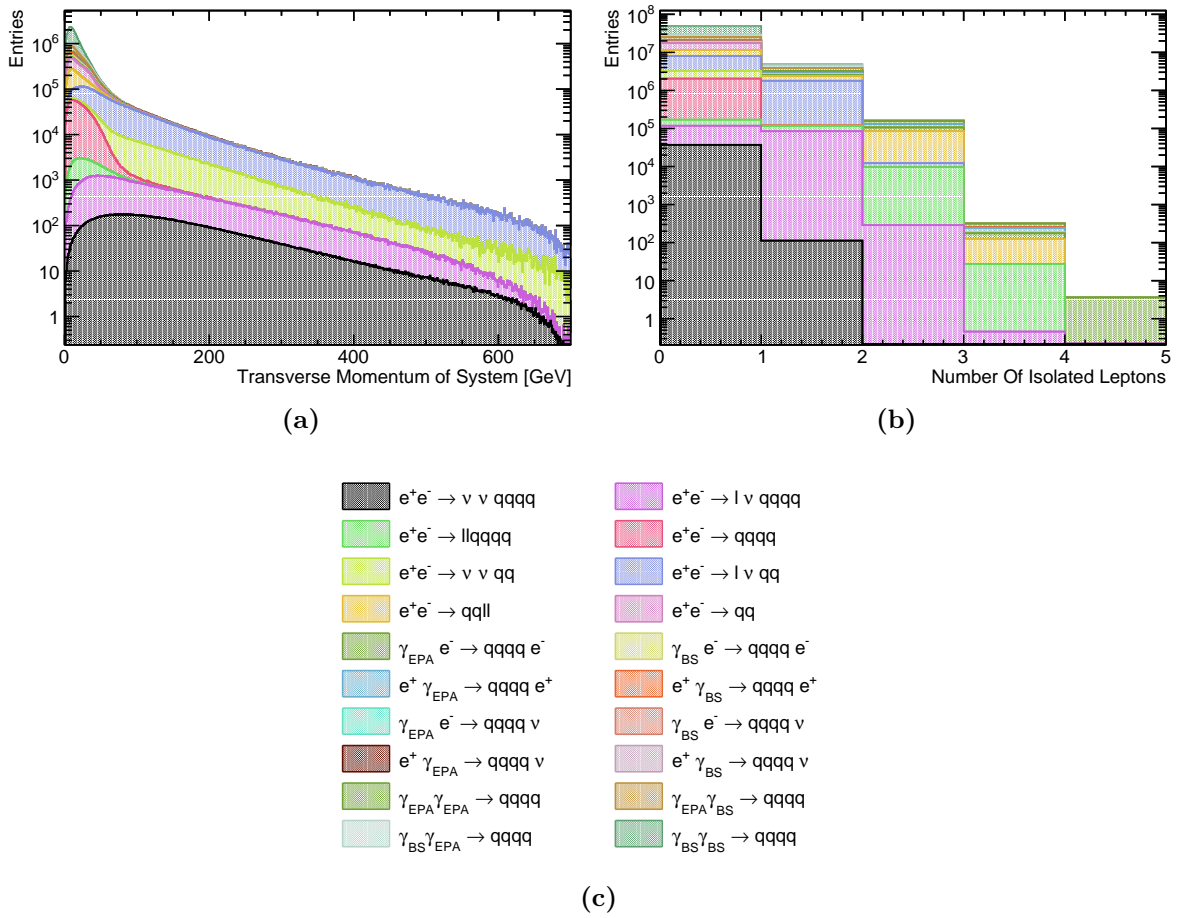The impact of these preselection cuts can be found in table 1.4 in section 1.5.3.

(a)

(b)

(c)

Figure 1.8: Distribution of variables cut on in the preselection at $\sqrt{s} = 1.4$ TeV. (a) The transverse momentum of the visible system. (b) The number of isolated leptons in the system. (c) The legend for the preceding plots.

1.5.2 Multivariate analysis

Having established the preselection cuts a MVA was applied, using the TMVA toolkit [18], to refine the event selection. The signal and background final state samples were halved;

one half sample was used to train the MVA and the remaining half sample was used in the subsequent analysis. The following variables were used for training of the MVA

- Number of PFOs in each jet.

- Energy of the highest energy PFO.

- Energy of the highest energy electron.

- Cosine of the polar angle of the highest energy track.

- Energy of the candidate bosons.

- Invariant mass of the candidate bosons.

- Acolinearity of the candidate boson pair.

- The vector sum of the transverse momentum of all PFOs in the event.

- The sphericity of the event.

- The derived jet clustering parameter variables $-\log_{10}(y_{ij})$ where y_{ij} are jet clustering parameters, $i = 3, 4$ and $j = i + 1$.

A variety of MVA options were considered and it was found that the optimal algorithm was the boosted decision tree (BDT) as shown by figure 1.9.

The BDT was further optimised by varying the number of trees used, the depth of the trees and the number of cuts applied. An optimal significance, $S/\sqrt{(S + B)}$ where S and B are the number of signal and background events passing the preselection respectively, of 52.7 was obtained.

1.5.3 Event Selection Summary

The event selection is summarised using the distribution of the invariant mass of the candidate bosons, which for the signal final state should peak around the W mass. This distribution is shown in figure 1.10 with no event selection, with the preselection cuts applied and with both preselections cuts and MVA applied. The event selection is also summarised using efficiencies shown in table 1.4.

As expected the dominant background processes after the MVA is applied are those that will look identical to the signal process, i.e. four primary quarks with missing energy.
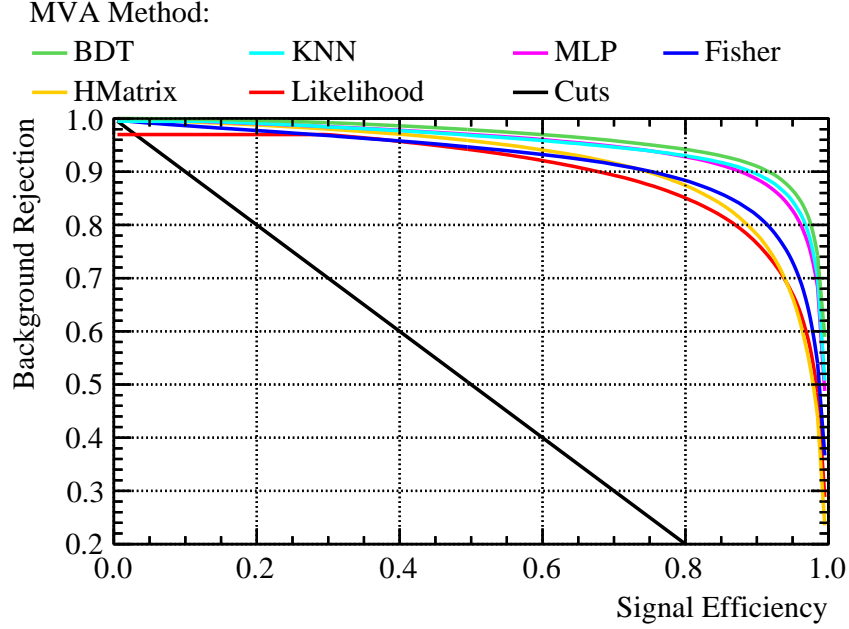
Figure 1.9: Background rejection as a function of signal efficiency for a variety of MVA options at $\sqrt{s} = 1.4$ TeV.

Two smaller sources of background are also present: two jet events with missing energy that are confused with four jet events with missing energy and events where a lepton is not properly reconstructed causing the event to look like four jets and missing energy.

1.6 Effect of Anomalous Coupling/Fitting Methodology

This section describes the procedure used for constructing the χ^2 surface and the subsequent confidence contours used to determine the sensitivity of CLIC to the anomalous gauge couplings α_4 and α_5.

1.6.1 Sensitive Distribution

The sensitivity of CLIC to the anomalous gauge couplings is determined through the use of a χ^2 fit to the distribution of M_{VV}, the invariant mass of the visible system. The
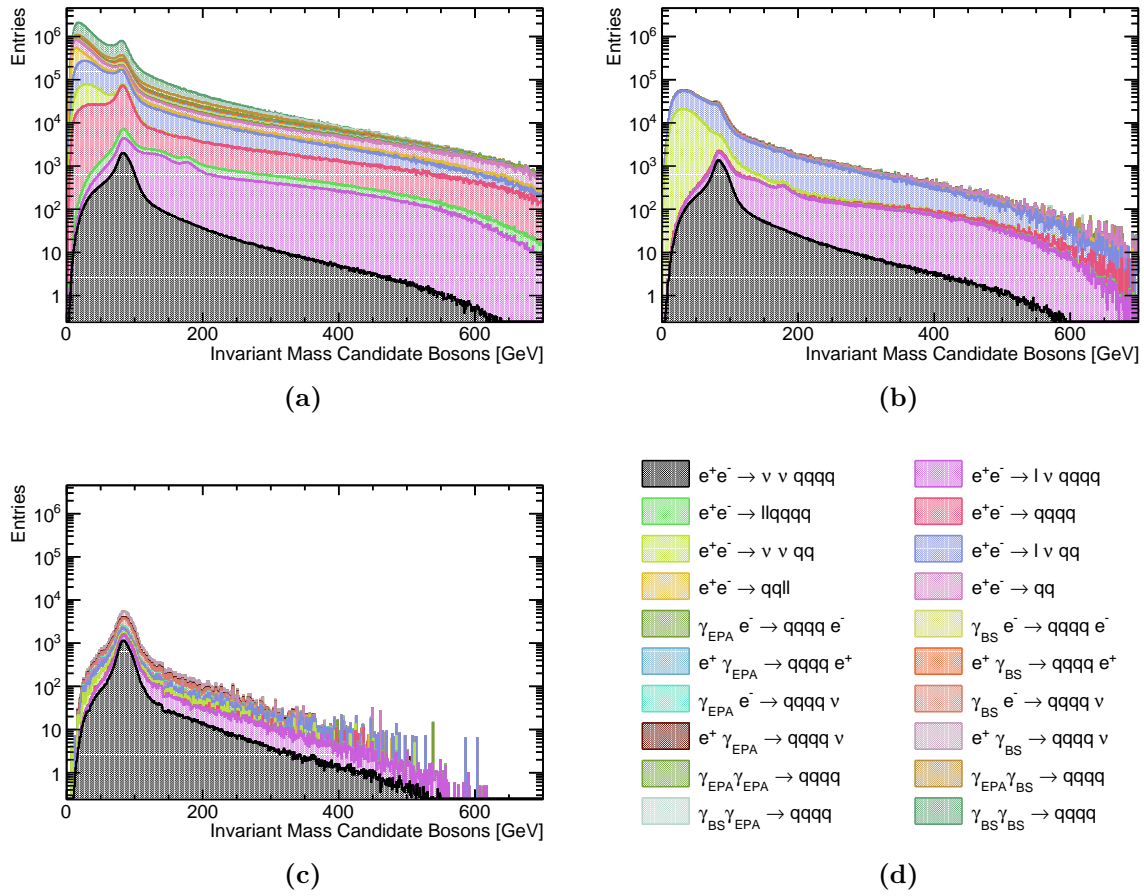
Figure 1.10: Impact of preselection and MVA on the reconstructed invariant mass of the bosons arising from jet pairing at $\sqrt{s} = 1.4$ TeV. (b) No cuts applied. (b) Preselection cuts applied. (c) MVA with preselection applied. (d) The legend for the event selection plots.

Final State	ϵ_{presel}	ϵ_{BDT}	N_{BDT}
$e^+e^- \to \nu\nu qqqq$	64.1%	44.5%	16,470
$e^+e^- \to l\nu qqqq$	26.1%	5.2%	8,582
$e^+e^- \to llqqqq$	0.8%	0.1%	100
$e^+e^- \to qqqq$	0.3%	0.1%	1,698
$e^+e^- \to \nu\nu qq$	43.4%	0.5%	5,351
$e^+e^- \to l\nu qq$	19.1%	0.1%	9,319
$e^+e^- \to llqq$	0.1%	-	234
$e^+e^- \to qq$	0.6%	-	1,586
$\gamma_{\text{EPA}}e^- \to qqqqe^-$	0.2%	-	48
$\gamma_{\text{BS}}e^- \to qqqqe^-$	0.1%	-	42
$e^+\gamma_{\text{EPA}} \to qqqqe^+$	0.3%	-	19
$e^+\gamma_{\text{BS}} \to qqqqe^+$	-	-	65
$\gamma_{\text{EPA}}e^- \to qqqq\nu$	26.0%	9.0%	4,421
$\gamma_{\text{BS}}e^- \to qqqq\nu$	36.1%	15.0%	23,150
$e^+\gamma_{\text{EPA}} \to qqqq\nu$	25.9%	9.2%	4,495
$e^+\gamma_{\text{BS}} \to qqqq\nu$	36.4%	15.3%	23,410
$\gamma_{\text{EPA}}\gamma_{\text{EPA}} \to qqqq$	0.2%	-	81
$\gamma_{\text{EPA}}\gamma_{\text{BS}} \to qqqq$	0.1%	-	55
$\gamma_{\text{BS}}\gamma_{\text{EPA}} \to qqqq$	-	-	53
$\gamma_{\text{BS}}\gamma_{\text{BS}} \to qqqq$	-	-	0

Table 1.4: Event selection efficiencies at $\sqrt{s} = 1.4$ TeV. In the above table, ϵ_{presel} denotes the number of events passing the preselection as a fraction of the total number of events, while ϵ_{BDT} denotes the number of events passing both the preselection and the BDT as a fraction of the total number of events. The EPA and BS subscript on the incoming photon indicates whether the photon is generated from the equivalent photon approximation or beamstrahlung. Cells omitting the efficiency indicate an efficiency of less than 0.1%.

distribution of M_{VV} proved to be highly sensitive to the anomalous gauge couplings, particularly for large M_{VV}, as shown in figure 1.11.

Two other variables were considered for this study, but they proved to be less sensitive to the anomalous gauge couplings than M_{VV}. They were $\cos\theta^*_{Jets}$, the angle between the boost direction and the back to back jets in the rest frame of the candidate bosons, and $\cos\theta^*_{Bosons}$, the angle between the boost direction and the back to back candidate bosons in the rest frame of the visible system. It should be noted that the distribution of $\cos\theta^*_{Jets}$

contains two entries per event, one for each candidate boson. To negate the effects of
correlation when determining sensitivity of the $\cos\theta^*_{Jets}$ variable, a two dimensional fit of
$\cos\theta^*_{Jets}$ was used where a distinction had been made between the candidate bosons based
on their energy. Figure 1.12 shows the sensitivity of these variables to the anomalous
gauge couplings. Of the variables considered, the M_{VV} distribution shows the greatest
sensitivity to the anomalous gauge couplings because the couplings primarily affect events
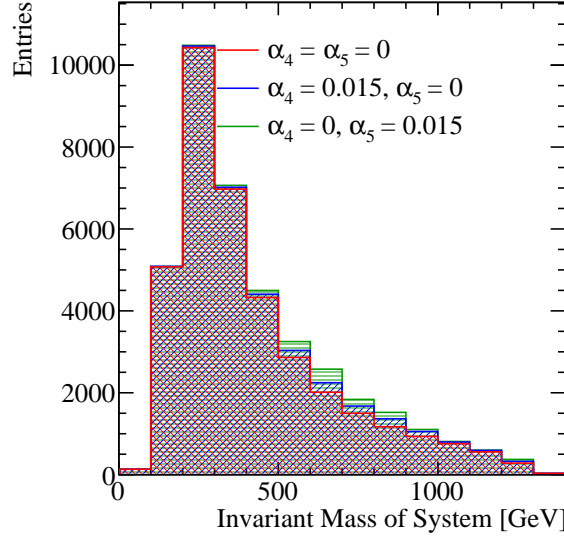with large values of M_{VV} and there are relatively few of these events.

Figure 1.11: The sensitivity of M_{VV} to the anomalous gauge couplings α_4 and α_5 at $\sqrt{s} =$
1.4 TeV. The jet algorithm used was the longitudinally invariant kt algorithm
with an R parameter of 0.9 and Selected PFOs were used. This distribution is
for the $\nu\nu$qqqq signal final state only.

1.6.2 χ^2 Surface and Confidence Limit Definition

A χ^2 surface is used to determine confidence limits on the anomalous gauge couplings
given the null hypothesis that $\alpha_4 = \alpha_5 = 0$. This surface is defined as

$$\chi^2 = \sum_i \frac{(O_i - E_i)^2}{E_i}, \tag{1.11}$$

where O_i is the observed, $\alpha_4 = \alpha_5 = 0$, and E_i the expected, $\alpha_4 \neq 0$ and $\alpha_5 \neq 0$, bin
content for bin i in the distribution of M_{VV}. The summation Σ_i runs over bins in the
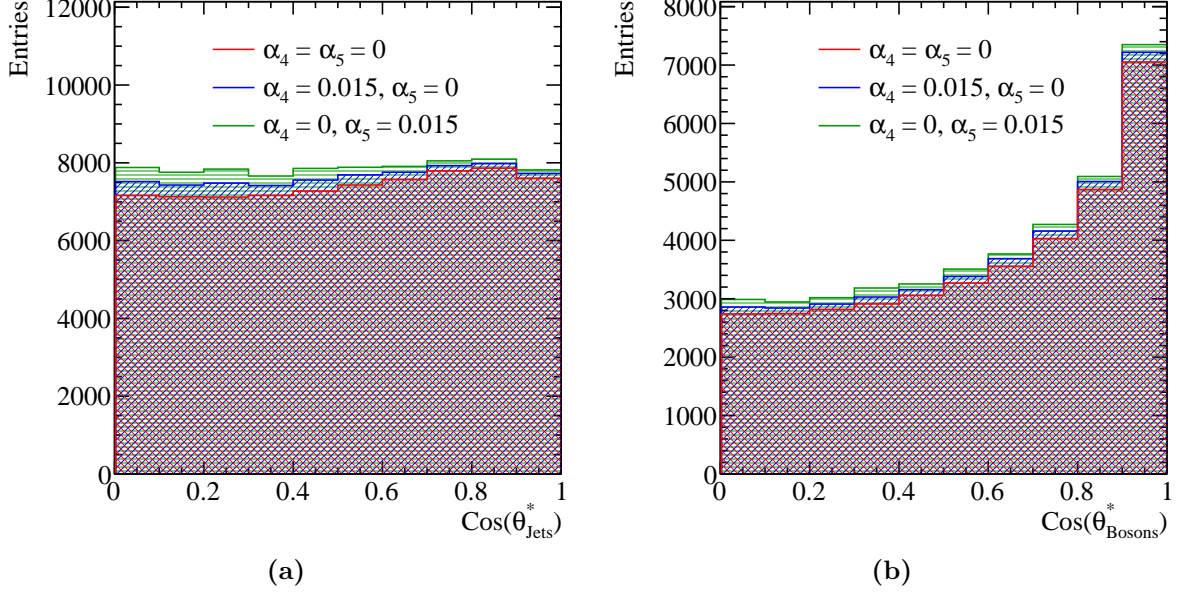M_{VV} distribution.

Figure 1.12: The sensitivity of various variables to the anomalous gauge couplings α_4 and α_5 at $\sqrt{s} = 1.4$ TeV. The jet algorithm used was the longitudinally invariant kt algorithm with an R parameter of 0.9 and Selected PFOs were used. This distribution is for the $\nu\nu$qqqq signal final state only. (a) shows the distribution of $\cos\theta^*_{Jets}$ and (b) shows the distribution of $\cos\theta^*_{Bosons}$.

The distribution of M_{VV} used to create the χ^2 surface was binned using 14 bins. The first bin spanned the invariant mass range between 0 and 200 GeV, this was followed by 11 bins of width 100 GeV ranging from 200 to 1300 GeV and finally the last bin contained all invariant masses above 1300 GeV. The expanded bin widths at the tails of the distribution were chosen to ensure the bin contents were sufficiently large to give a reliable estimate the likelihood function using the χ^2 parameter. This choice of bin width ensured the bin contents were sufficiently large to minimise fluctuations arising from individual events with large weights.

Confidence limits describing the sensitivity of the CLIC experiment to the anomalous gauge couplings were found by examining the χ^2 surface in the space of α_4 and α_5. Deviations from the minima of this surface, which by construction occurs at $\alpha_4 = \alpha_5 = 0$, yield confidence limits that indicate the probability of observing a particular value of α_4 and α_5 given the null hypothesis that $\alpha_4 = \alpha_5 = 0$. The confidence limits reported in subsequent sections, 68%, 90% and 99%, are defined using fixed deviations from the minima of χ^2 surface ($\Delta\chi^2$) of 2.28, 4.61 and 9.21 respectively.

Confidence limits on the individual parameters α_4 and α_5 were determined by setting the corresponding coupling term to zero and examining the remaining one dimensional χ^2 distribution. A fourth order polynomial was fitted to the minima of this distribution and the one sigma confidence limit defined using $\Delta\chi^2 = 1$. The definition of a one sigma confidence limit accounts for changes in the number of degrees of freedom in the fit, therefore, it changes when fixing the corresponding coupling term to zero.

1.6.3 Event Weight Interpolation Scheme

In order to obtain a smooth χ^2 surface a fine sampling of the event weights in the α_4 and α_5 space is required, however, it is unfeasible to generate a finely sampled grid of event weights on an event by event basis because event generation is highly CPU intensive. To resolve this issue, an interpolation scheme was applied to determine the event weights within a sampled region of the α_4 and α_5 space. This allows for an infinite sampling of the event weights in the space of α_4 and α_5 without having to call the generator an infinite number of times.

A bicubic interpolation scheme, cubic interpolation along the two dimensions, was applied to the event weights produced by the generator. This procedure is best illustrated by figure 1.13, which shows the interpolated event weight surface superimposed with the raw event weights from the generator for four $\nu\nu$qqqq events at $\sqrt{s} = 1.4$ TeV. This interpolation scheme produces a smooth and continuous surface that can be used for generating a smooth χ^2 surface.

1.7 Results

The sensitivity of the CLIC experiment to the anomalous gauge couplings α_4 and α_5 at $\sqrt{s} = 1.4$ TeV is shown in figure 1.14a. This result shows the sensitivity after the application of preselection and MVA purposed to remove the included background channels. These contours yield the one σ confidence limits for CLIC operating at $\sqrt{s} = 1.4$ TeV of

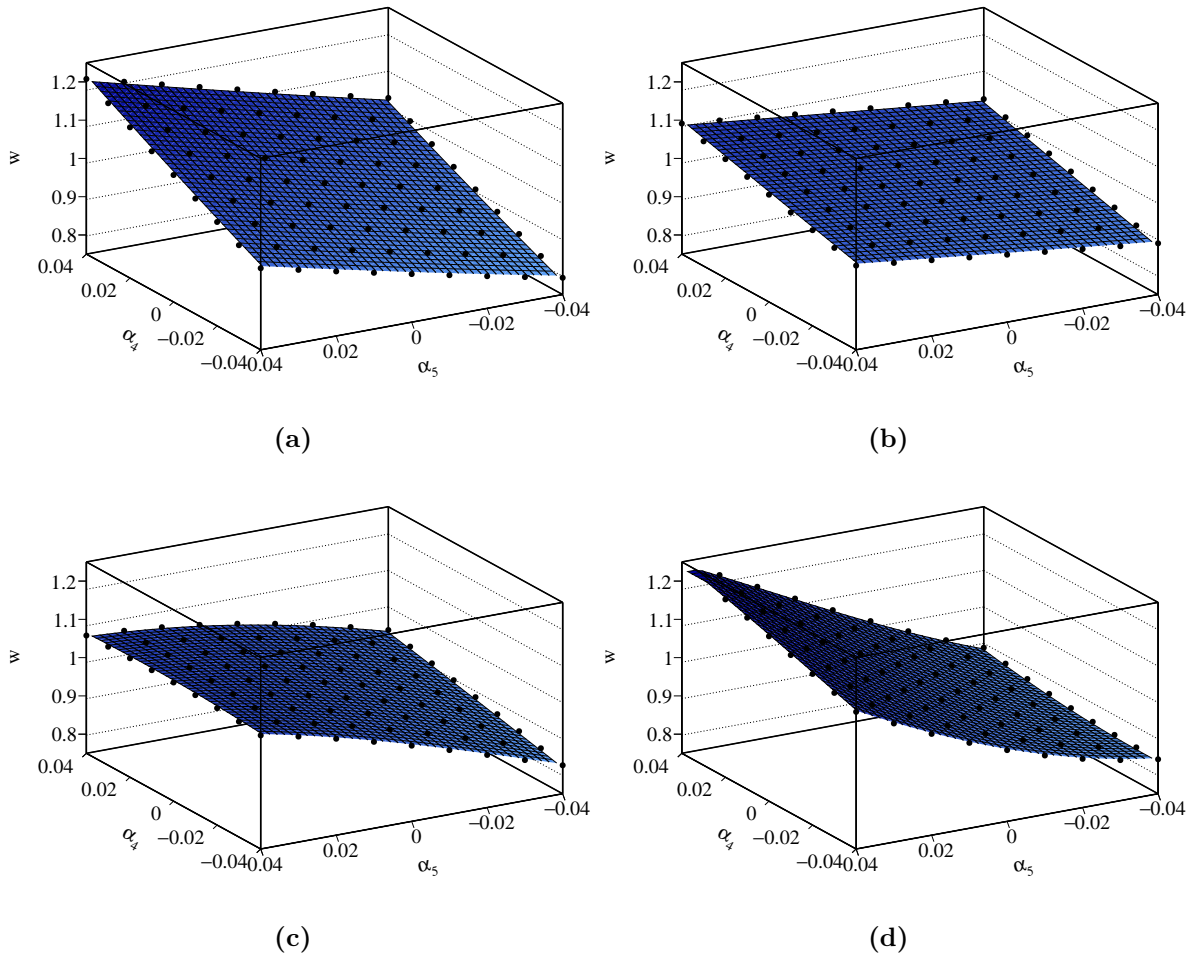$$-0.0082 < \alpha_4 < 0.0116 \tag{1.12}$$

Figure 1.13: A selection of plots showing how the event weight changes when varying the anomalous couplings α_4 and α_5 for $\sqrt{s} = 1.4$ TeV $\nu\nu$qqqq final state events. The hollow circles show the event weight produced from the generator, while the surface shown is found using bicubic interpolation between those points.

and

$$-0.0055 < \alpha_5 < 0.0078. \tag{1.13}$$

1.7.1 Systematic Uncertainties

A source of systematic error in this experiment is the uncertainty on the cross sections for the signal and background final states. Based on the selection efficiencies given in table 1.4, the distribution used to determine the sensitivity of CLIC to the anomalous gauge
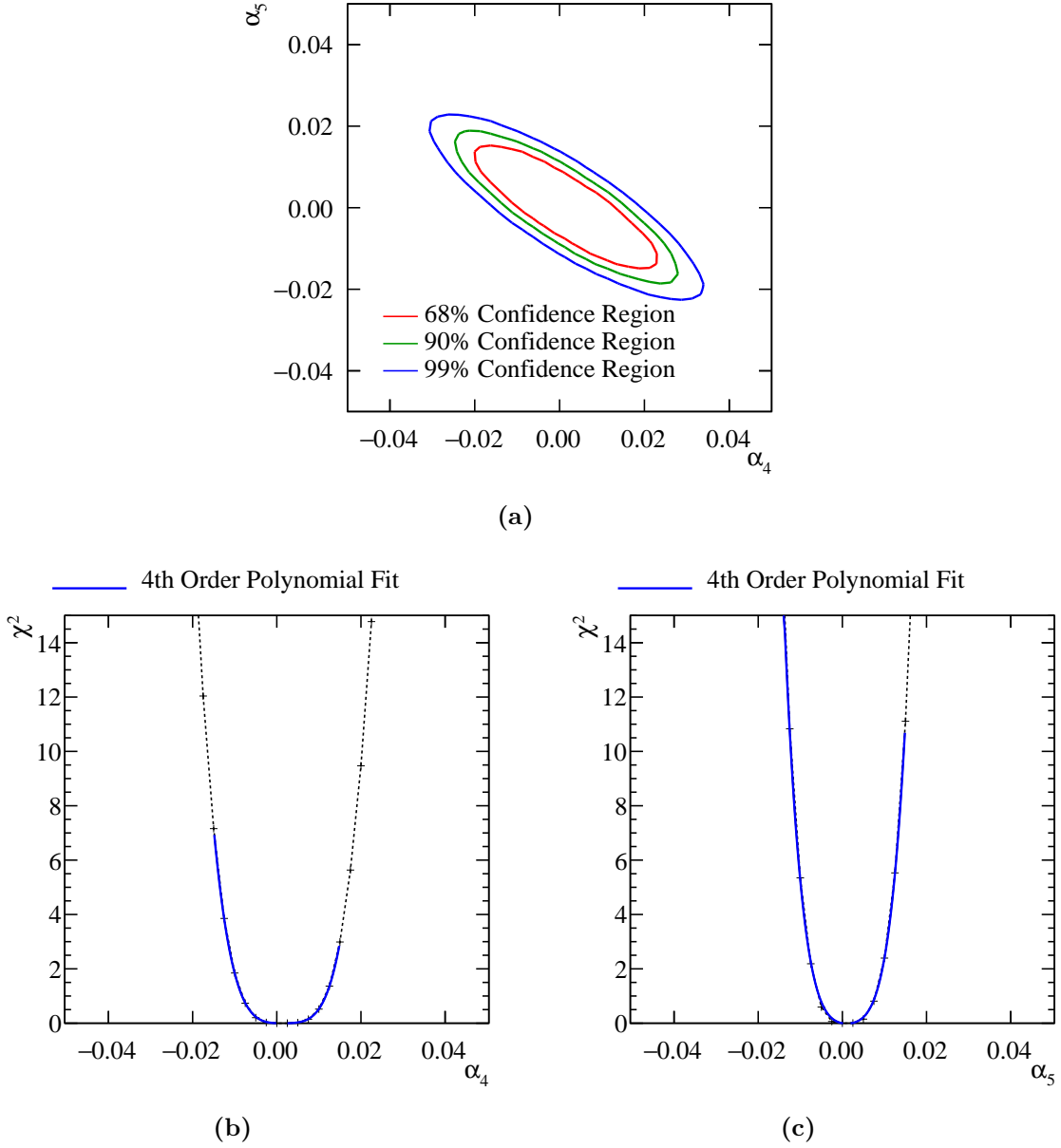
Figure 1.14: χ^2 sensitivity distributions from a fit to M_{VV} at $\sqrt{s} = 1.4$ TeV. Results include the effect of backgrounds after the application of a series of preselection cuts and MVA. (a) χ^2 sensitivity contours in α_4 and α_5 space. (b) χ^2 as a function of α_4 assuming $\alpha_5 = 0$. (c) χ^2 as a function of α_5 assuming $\alpha_4 = 0$.

couplings primarily consists of $\gamma_{\mathrm{BSE}}\mathrm{e}^{\pm} \to \mathrm{qqqq}\nu$ events, therefore, uncertainties on the cross section for these processes should be considered. A detailed study of these processes is yet to be undertaken for CLIC, therefore, a broad span of cross section uncertainties is considered for completion.

The effect of the uncertainty on the $\gamma_{\mathrm{BS}}\mathrm{e}^{\pm} \to \mathrm{qqqq}\nu$ cross sections is included in the χ^2 through the use of a nuisance parameter. The cross section for the $\gamma_{\mathrm{BS}}\mathrm{e}^{\pm} \to \mathrm{qqqq}\nu$ processes are allowed to fluctuate, however, the magnitude of the fluctuation, r, is moderated by an additional penalty term in the χ^2 as follows:

$$\chi^2(r) = \sum_i \frac{(O_i - E_i(r))^2}{E_i(r)} + \frac{(r-1)^2}{\sigma_r^2}, \qquad (1.14)$$

where O_i is the observed, $\alpha_4 = \alpha_5 = 0$, bin content for bin i in the distribution of M_{VV} with no background fluctuations. $E_i(r)$ is the expected, $\alpha_4 \neq 0$ and $\alpha_5 \neq 0$, bin content for bin i in the distribution of M_{VV} with the $\gamma_{\mathrm{BS}}\mathrm{e}^{\pm} \to \mathrm{qqqq}\nu$ background cross sections fluctuated by the factor r. $\sum_i$ is the sum over the bins of the M_{VV} distribution. The σ_r variable is the width of the distribution of r, which indicates the uncertainty on the measurement of the background cross sections. The χ^2 surface is constructed in the space of α_4 and α_5 by minimising $\chi^2(r)$ at each point. The 68% confidence contour is shown with the inclusion of this nuisance parameter for various values of σ_r in figure 1.15.
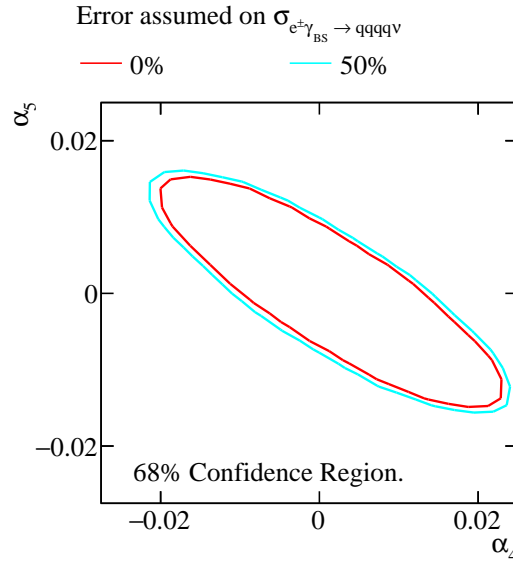

Figure 1.15: 68% sensitivity contour including systematic errors, of varying magnitudes, in dominant background cross sections.

Minimal changes in sensitivity are observed when allowing the backgrounds to fluctuate even up to the 50% level. This can be understood by considering the shape of the M_{VV} distribution for the signal and the $\gamma_{\mathrm{BS}}\mathrm{e}^{\pm} \to \mathrm{qqqq}\nu$ backgrounds, which is shown in figure 1.16. These distribution shows that anomalous couplings primarily affect events with

large invariant masses, while these backgrounds peak at low invariant masses. Therefore, by fluctuating the cross-section for the background processes, it is not possible to gain a significantly better match between the observed and expected bin contents in the M_{VV} distribution. This is encouraging as despite these backgrounds dominating the χ^2 fit that determinea the sensitivity of CLIC to the anomalous gauge couplings, precise knowledge of their cross-section is not crucial.
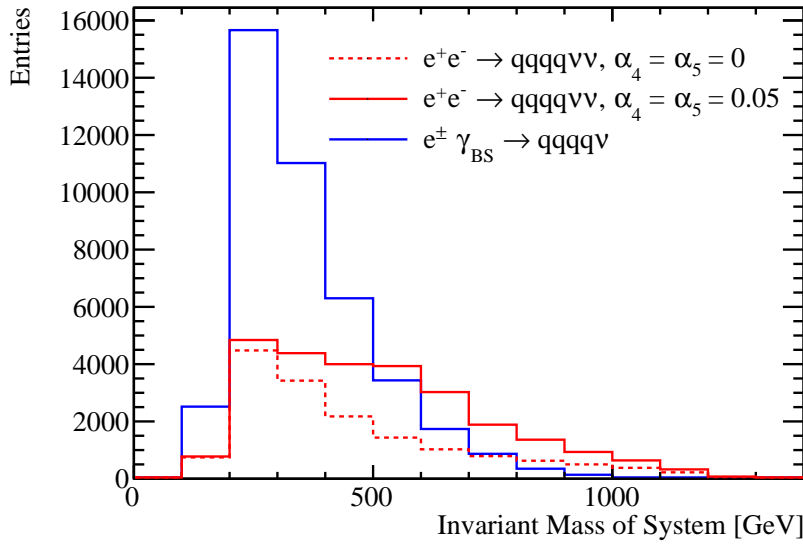

Figure 1.16: Distributions of M_{VV} for the $\nu\nu$qqqq, with and without the effect from anomalous couplings, and the combined dominant background processes $\gamma_{\rm BS}{\rm e}^{\pm} \to {\rm qqqq}\nu$.

1.8 Sensitivity at $\sqrt{s} = 3$ TeV

The anomalous gauge coupling sensitivity study described in this chapter was repeated for CLIC operating at $\sqrt{s} = 3$ TeV. As this analysis largely mirrors that of the $\sqrt{s} = 1.4$ TeV analysis, this section focuses on the differences between the two analyses.

The signal and background final states for the $\sqrt{s} = 3$ TeV analysis were identical to those used for the $\sqrt{s} = 1.4$ TeV analysis. Cross sections for these processes at $\sqrt{s} = 3$ TeV are given in table 1.5.

The data analysis and event selection procedures used at $\sqrt{s} = 3$ TeV mirrored those used at $\sqrt{s} = 1.4$ TeV. Descriptions of both can be found in sections 1.4 and 1.5 respectively.

Final State	Cross Section $\sqrt{s} = 3$ TeV [fb]
$e^+e^- \rightarrow \nu\nu qqqq$	71.5
$e^+e^- \rightarrow l\nu qqqq$	106.6
$e^+e^- \rightarrow llqqqq$	169.3
$e^+e^- \rightarrow qqqq$	546.5
$e^+e^- \rightarrow \nu\nu qq$	1317.5
$e^+e^- \rightarrow l\nu qq$	5560.9
$e^+e^- \rightarrow llqq$	3319.6
$e^+e^- \rightarrow qq$	2948.9
$\gamma_{\text{EPA}}e^- \rightarrow qqqqe^-$	287.8
$\gamma_{\text{BS}}e^- \rightarrow qqqqe^-$	1268.6
$e^+\gamma_{\text{EPA}} \rightarrow qqqqe^+$	287.8
$e^+\gamma_{\text{BS}} \rightarrow qqqqe^+$	1267.3
$\gamma_{\text{EPA}}e^- \rightarrow qqqq\nu$	54.2
$\gamma_{\text{BS}}e^- \rightarrow qqqq\nu$	262.5
$e^+\gamma_{\text{EPA}} \rightarrow qqqq\nu$	54.2
$e^+\gamma_{\text{BS}} \rightarrow qqqq\nu$	262.3
$\gamma_{\text{EPA}}\gamma_{\text{EPA}} \rightarrow qqqq$	402.7
$\gamma_{\text{EPA}}\gamma_{\text{BS}} \rightarrow qqqq$	2423.1
$\gamma_{\text{BS}}\gamma_{\text{EPA}} \rightarrow qqqq$	2420.6
$\gamma_{\text{BS}}\gamma_{\text{BS}} \rightarrow qqqq$	13050.3

Table 1.5: Cross sections of signal and background processes at $\sqrt{s} = 3$ TeV. In the above table q represents u, $\bar{\text{u}}$, d, $\bar{\text{d}}$, s, $\bar{\text{s}}$, c, $\bar{\text{c}}$, b or $\bar{\text{b}}$; l represents $e^{\pm}$, $\mu^{\pm}$ or $\tau^{\pm}$; and ν represents ν_e, $\overline{\nu_e}$, ν_μ, $\overline{\nu_\mu}$, ν_τ and $\overline{\nu_\tau}$. The EPA and BS subscript on the incoming photon indicates whether the photon is generated from the equivalent photon approximation or beamstrahlung.

Jet finding was performed using the longitudinally invariant k_t algorithm as described in section . The jet algorithm configuration was optimised using the sensitivity of CLIC to the anomalous gauge couplings using pure signal only as described in section 1.4.2.1. The optimal jet algorithm configuration at $\sqrt{s} = 3$ TeV used tight selected PFOs and an R parameter of 1.1. The one sigma confidence limits using pure signal and this jet algorithm configuration were

$$-0.0003 < \alpha_4 < 0.0003 \tag{1.15}$$

and

$$-0.0002 < \alpha_5 < 0.0002. \qquad (1.16)$$

These limits represent the upper bound on the sensitivity of the CLIC experiment to the anomalous gauge couplings at $\sqrt{s} = 3$ TeV. As the cross section for the $\gamma\gamma \to hadrons$ increases with energy, the effect of these background is more problematic at $\sqrt{s} = 3$ TeV than at $\sqrt{s} = 1.4$ TeV [14]. Therefore, it is to be expected that the optimal PFO selection at $\sqrt{s} = 3$ TeV, tight selected PFOs, is more aggressive at vetoing these backgrounds than at $\sqrt{s} = 1.4$ TeV, selected PFOs, which is what is observed.

As opposed to training the MVA using 50% of the signal and background events, as was done for the $\sqrt{s} = 1.4$ TeV analysis, the $\sqrt{s} = 3$ TeV analysis trained the MVA using 10% of the signal and background events. This modification minimises the effect of events with large weights that would otherwise skew the M_{VV} distribution and bias the fit. No such effect was seen at $\sqrt{s} = 1.4$ TeV where the sensitivity to anomalous couplings is much lower. The sample sizes were sufficiently large that training on 10% of the total sample was sufficient to achieve good MVA performance. Event selection for the $\sqrt{s} = 3$ TeV analysis is summarised in table 1.6.

Due to the increased sensitivity of the signal sample, event weights were sampled with greater frequency in the space of α_4 and α_5 at $\sqrt{s} = 3$ TeV than at $\sqrt{s} = 1.4$ TeV analysis. Bicubic interpolation was again used to make a continuous surface for the event weights. These event weight surfaces were then used to construct the M_{VV} distribution and the χ^2 surface used to determine the reported sensitivities. Figure 1.17 shows an example of the event weights extracted from the generator and the interpolated surface used to define the χ^2 surface as a function of α_4 and α_5 for a selected $\nu\nu$qqqq event at $\sqrt{s} = 3$ TeV.

The sensitivity of the CLIC experiment to the anomalous gauge couplings α_4 and α_5 at $\sqrt{s} = 3$ TeV is shown in figure 1.18a. This result shows the sensitivity after the application of preselection and MVA, described in sections 1.5.1 and 1.5.2, purposed to remove the included background channels. These contours yield the one σ confidence limit on the measurement of

$$-0.0010 < \alpha_4 < 0.0011 \qquad (1.17)$$

Final State	ϵ_{presel}	ϵ_{BDT}	N_{BDT}
$e^+e^- \to \nu\nu qqqq$	74.4%	46.0%	65,740
$e^+e^- \to l\nu qqqq$	40.0%	12.0%	25,660
$e^+e^- \to llqqqq$	7.5%	1.1%	3,570
$e^+e^- \to qqqq$	3.7%	0.3%	3,224
$e^+e^- \to \nu\nu qq$	50.5%	1.2%	30,510
$e^+e^- \to l\nu qq$	32.0%	0.4%	48,320
$e^+e^- \to llqq$	1.4%	-	1,028
$e^+e^- \to qq$	1.4%	0.1%	3,268
$\gamma_{\text{EPA}}e^- \to qqqqe^-$	6.6%	0.8%	4,736
$\gamma_{\text{BS}}e^- \to qqqqe^-$	4.6%	0.7%	13,660
$e^+\gamma_{\text{EPA}} \to qqqqe^+$	6.5%	0.8%	4,686
$e^+\gamma_{\text{BS}} \to qqqqe^+$	4.7%	0.7%	13,310
$\gamma_{\text{EPA}}e^- \to qqqq\nu$	45.6%	17.2%	18,610
$\gamma_{\text{BS}}e^- \to qqqq\nu$	55.9%	26.7%	110,900
$e^+\gamma_{\text{EPA}} \to qqqq\nu$	45.9%	17.3%	18,750
$e^+\gamma_{\text{BS}} \to qqqq\nu$	56.5%	27.4%	113,700
$\gamma_{\text{EPA}}\gamma_{\text{EPA}} \to qqqq$	5.3%	0.7%	5,531
$\gamma_{\text{EPA}}\gamma_{\text{BS}} \to qqqq$	3.5%	0.4%	16,640
$\gamma_{\text{BS}}\gamma_{\text{EPA}} \to qqqq$	3.5%	0.4%	15,900
$\gamma_{\text{BS}}\gamma_{\text{BS}} \to qqqq$	0.6%	-	4,124

Table 1.6: Event selection efficiencies at $\sqrt{s} = 3$ TeV. In the above table, ϵ_{presel} denotes the number of events passing the preselection as a fraction of the total number of events, while ϵ_{BDT} denotes the number of events passing both the preselection and the BDT as a fraction of the total number of events. The EPA and BS subscript on the incoming photon indicates whether the photon is generated from the equivalent photon approximation or beamstrahlung. Cells omitting the efficiency indicate an efficiency of less than 0.1%.
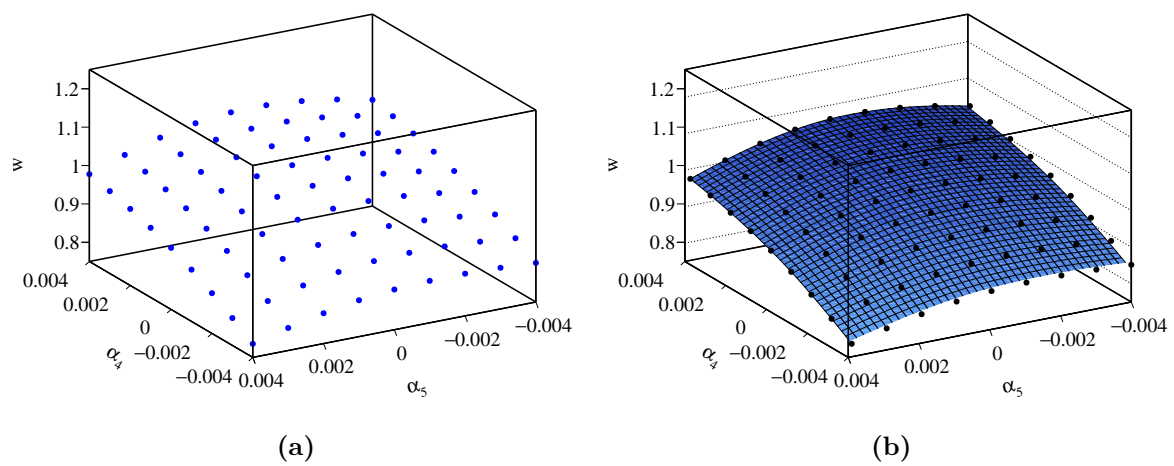
and

$$-0.0007 < \alpha_5 < 0.0007. \tag{1.18}$$

(a)   **(b)**
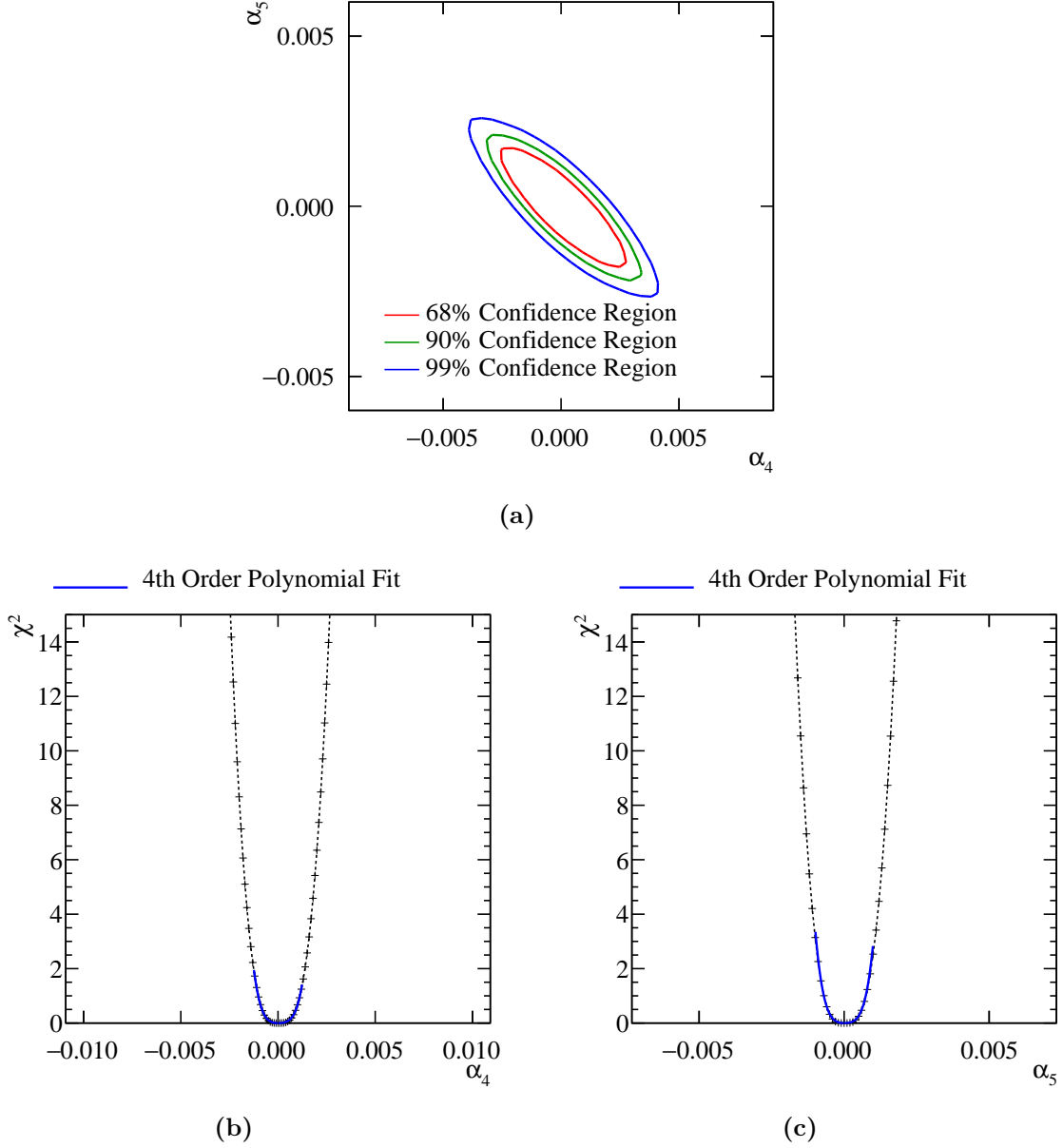
Figure 1.17: FILL IN

Figure 1.18: χ^2 sensitivity distributions from a fit to M_{VV} at $\sqrt{s} = 3$ TeV. Results include the effect of backgrounds after the application of a series of preselection cuts and MVA. (a) χ^2 sensitivity contours in α_4 and α_5 space. (b) χ^2 as a function of α_4 assuming $\alpha_5 = 0$. (c) χ^2 as a function of α_5 assuming $\alpha_4 = 0$.

Colophon

This thesis was made in LaTeX 2$_\varepsilon$ using the "hepthesis" class [19].

Bibliography

[1] E. Fermi. An attempt of a theory of beta radiation. 1. *Z. Phys.*, 88:161–177, 1934.

[2] Georges Aad et al. Evidence for Electroweak Production of $W^{\pm}W^{\pm}jj$ in pp Collisions at $\sqrt{s} = 8$ TeV with the ATLAS Detector. *Phys. Rev. Lett.*, 113(14):141803, 2014.

[3] J. Beringer et al. Review of Particle Physics (RPP). *Phys. Rev.*, D86:010001, 2012.

[4] Wolfgang Kilian, Thorsten Ohl, and Jurgen Reuter. WHIZARD: Simulating Multi-Particle Processes at LHC and ILC. *Eur. Phys. J.*, C71:1742, 2011.

[5] Mauro Moretti, Thorsten Ohl, and Jurgen Reuter. O'Mega: An Optimizing matrix element generator. 2001.

[6] Torbjorn Sjostrand, Stephen Mrenna, and Peter Z. Skands. PYTHIA 6.4 Physics and Manual. *JHEP*, 05:026, 2006.

[7] G. Alexander et al. A Comparison of b and u d s quark jets to gluon jets. *Z. Phys.*, C69:543–560, 1996.

[8] Z. Was. TAUOLA the library for tau lepton decay, and KKMC / KORALB / KORALZ /... status report. *Nucl. Phys. Proc. Suppl.*, 98:96–102, 2001. [,96(2000)].

[9] Toshinori Abe et al. The International Large Detector: Letter of Intent. 2010.

[10] P. Mora de Freitas and H. Videau. Detector simulation with MOKKA / GEANT4: Present and future. In *Linear colliders. Proceedings, International Workshop on physics and experiments with future electron-positron linear colliders, LCWS 2002, Seogwipo, Jeju Island, Korea, August 26-30, 2002*, pages 623–627, 2002.

[11] S. Agostinelli et al. GEANT4: A Simulation toolkit. *Nucl. Instrum. Meth.*, A506:250–303, 2003.

[12] F. Gaede. Marlin and LCCD: Software tools for the ILC. *Nucl. Instrum. Meth.*,

A559:177–180, 2006.

[13] M. A. Thomson. Particle Flow Calorimetry and the PandoraPFA Algorithm. *Nucl. Instrum. Meth.*, A611:25–40, 2009.

[14] J. S. Marshall, A. Münnich, and M. A. Thomson. Performance of Particle Flow Calorimetry at CLIC. *Nucl. Instrum. Meth.*, A700:153–162, 2013.

[15] Lucie Linssen, Akiya Miyamoto, Marcel Stanitzki, and Harry Weerts. Physics and Detectors at CLIC: CLIC Conceptual Design Report. 2012.

[16] W. Kilian. WHIZARD 1.0: A generic Monte-Carlo integration and event generation package for multi-particle processes.

[17] Matteo Cacciari, Gavin P. Salam, and Gregory Soyez. FastJet User Manual. *Eur. Phys. J.*, C72:1896, 2012.

[18] Andreas Hoecker, Peter Speckmayer, Joerg Stelzer, Jan Therhaag, Eckhard von Toerne, and Helge Voss. TMVA: Toolkit for Multivariate Data Analysis. *PoS*, ACAT:040, 2007.

[19] Andy Buckley. The hepthesis LaTeX class.